Desalination and Water Treatment
www.deswater.com

doi: 10.5004/dwt.2022.29116

280 (2022) 188–196
December

Synthesis and characterization studies on the degradation of Rhodamine B from aqueous solution by Cu-NiO/AC nanocomposites

R. Vaithianathan*, P. Anitha, T. Venugopal, A. Ramachandran

Centre for Research, Department of Chemistry, Government College of Engineering, Salem 636011, Tamil Nadu, India, emails: rvnkishan@gmail.com (R. Vaithianathan), anitha1180@gmail.com (P. Anitha), t.venu1973@gmail.com (T. Venugopal), rams.anbu@gmail.com (A. Ramachandran)

Received 20 June 2022; Accepted 4 November 2022

ABSTRACT

Using the novel reflux-thermal method, a novel nanocomposite was prepared from activated carbon of *Zea mays* L. waste with copper-nickel-oxide (ZMCN). Nickel sulfate ($NiSO_4$) and copper sulfate ($CuSO_4$) were used as metal sources with $NaBH_4$ and NaOH as a precursor. The composite was characterized by Brunauer–Emmett–Teller, Fourier-transform infrared spectroscopy (FT-IR), X-ray diffraction (XRD), scanning electron microscopy (SEM), high-resolution transmission electron microscopy, and thermogravimetric analysis/differential thermal analysis. The morphological characteristics of the synthesized ZMCN have been characterized using SEM. The XRD analysis showed the crystalline nature of ZMCN nanocomposite. In addition, FT-IR and energy-dispersive X-ray spectroscopy analyses were also carried out to investigate the particle size, chemical functional group, and elemental composition of ZMCN. The ZMCN was subsequently used for the dye degradation of Rhodamine B (RhB) at room temperature. RhB degradation was found to be 98.7% in 50 mg/L solution.

Keywords: Copper-nickel-oxide; Rhodamine B; Dye degradation; Catalyst

1. Introduction

Nanocrystalline Cu-NiO loaded activated carbon, because of its moderately low cost, non-toxicity, good opto-electronic properties, and excellent chemical stability has potential applications in photocatalytic degradation of toxic pollutants dispersed in the environment. Nowadays, water contamination by different pollutants (mainly heavy metals and dyes) has become a major environmental problem and a threat to the well-being of living organisms [1–5]. Heavy metals and dyes that are widely distributed in the environment remain non-biodegradable, persistent, carcinogenic, and toxic. They bioaccumulate in living organisms through the food chain, and their accumulation causes different diseases and malfunctions. Many efforts have been devoted to designing different adsorbents for removing colored dyes. Wastewater treatment using a small amount of an adsorbent could remove a large amount of dye [6–11]. Since activated carbon is one of the most used adsorbents with a porous structure, an enormous specific surface area, and strong adsorption capacity, it is widely used to remove organic dyes and pollutants from industrial wastewater [12–16]. Activated carbon can adsorb many dyes with a high adsorption capacity, but its adsorption efficiency is low [17–23].

Currently, advanced oxidation processes (AOPs), that employ eco-friendly hydrogen peroxide (H_2O_2), are characterized by a common feature; the capability of exploiting high reactive oxidizing agents such as hydroxyl radicals ($^{\bullet}OH$) to destroy most organic pollutants (e.g., dyes) present in wastewater completely. The use of metal oxide nanoparticles is restricted because recovery of the metal oxide from the degraded dye solution cannot be accomplished completely. The magnetic method fails to remove the metal oxide nanoparticles entirely. When released into the environment,

* Corresponding author.

these metal oxides cause heavy metal pollution; hence, their removal is imperative. Activated carbon-supported metal oxide can be removed easily after the degradation by a simple centrifugation technique [8]. Activated carbon, in some cases, was found to absorb the degraded product of the dye. This study focuses on using activated carbon to support the metal oxide.

In this research work, a copper-nickel-oxide-loaded activated carbon (ZMCN) photocatalyst was prepared. Various studies were made and the resulting ZMCN was characterized. The research aimed to investigate the photocatalytic activity of ZMCN on Rhodamine B solution under UV-radiation. The ZMCN was characterized by Brunauer–Emmett–Teller (BET), Fourier-transform infrared spectroscopy (FT-IR), X-ray diffraction (XRD), scanning electron microscopy (SEM), and thermogravimetric analysis/differential thermal analysis (TGA/DTA). This investigation could support the analysis of the possibility of employing ZMCN for removing textile dyes.

2. Experimental method

2.1. Materials

Waste from the *Zea mays* L. plant was gathered in Karupur, Tamil Nadu, India. The outer covering of the gathered wastes was removed before washing and the samples were dried at room temperature for 3–4 d to eliminate all moisture. Dried wastes were ground to a fine powder and stored in a dry, airtight container for later use. Sulfuric acid, hydrochloric acid, sodium hydroxide, copper sulfate, and nickel sulfate were acquired from Merck (India) and were utilized in their unaltered form.

2.2. Preparation of ZMCN

Zea mays L trash was used to make activated carbon from biowaste sources. Waste from *Zea mays* L was thoroughly washed with distilled water and dried at 100°C for 24 h. A two-step physico-chemical method was used to activate the dried material [24]. Physical activation was followed by H_2SO_4 with HNO_3 activation in a two-step activation procedure. To obtain the raw enhanced activated carbon (AC) in ash form, the dried *Zea mays* L waste was burned in a muffle furnace at a high temperature of 600°C. First, AC was thoroughly cleaned with distilled water before being immersed in 60% sulfuric acid and 30% HNO_3 in the ratio of 1:2 and then purged with N_2 for 6 h to digest it. The resultant mass was then thoroughly cleaned with plenty of water. Next, AC was cleaned thoroughly with plenty of hot water to eliminate the excess acid. The dried carbon is then ground for 10 min in a planetary ball mill with zirconium balls to achieve a consistent size of carbon.

The activated carbon (AC) was loaded with copper-nickel-oxide nanoparticles. First, 1 g of AC was disseminated in 600 mL of distilled water at room temperature for 2 h using sonication. Next, 20 mL of 1 N copper sulfate and 20 mL of 1 N nickel sulfate were added. The metal ions solution was then reduced with 0.025 N of $NaBH_4$, and 1 N NaOH was added drop by drop. Next, the solution was refluxed in a magnetic stirrer bath for 8 h in a nitrogen environment (Fig. 1). Finally, ZMCN was filtered and washed with distilled water and ethanol before drying at room temperature for 5 h.

3. Result and discussions

3.1. X-Ray diffraction studies

Fig. 2a depicts the X-ray diffraction peaks for ZMCN composites at 2θ = 37, 41, and 43 due to the orthorhombic structure [24]. Fig. 2b shows the XRD of activated carbon. There is no characteristic peak in the activated carbon which indicates the amorphous nature of the carbon. In Fig. 2a, metallic copper (Cu(0)) diffraction peaks at 2θ = 37, 41, and 43 were assigned to the (111), (031), and (130) planes and NiO peaks at 2θ = 12.34, 17.55, and 23.45 were assigned to the (111), (031), and (130) planes, respectively. These results were matched with observed values in JCPDS files (No. 01-078-0648 and No. 00-049-1830, respectively) [25] for ZMCN. Cu and NiO were ascribed to all diffraction peaks, showing that only Cu and NiO were formed in the current system. The diffraction peaks of NiO were dramatically amplified with the addition of activated carbon. Therefore, the overlap of the peaks attributes to the little distance between them instead of the formation of alloys. The absence of additional distinctive peaks owing to contaminants and sharp peaks in the pattern, as shown in Fig. 2, indicates that the produced samples were of high purity and crystallinity. According to the full-width at half-maximum values of diffraction peaks and Debye-equation, Scherrer's average crystallite size of ZMCN was effectively determined [26]. The average crystallite size for ZMCN was found to be 39.34 nm.

3.2. Scanning electron microscopy

Fig. 3 shows the SEM micrograph pictures of activated carbon and ZMCN before and after dye degradation. An SEM image vividly demonstrates the shape and structure of the nanocomposite under investigation. AC has a porous structure with a smooth surface (Fig. 3a), but Fig. 3b of ZMCN shows that the nanocomposite was agglomerated and fixed to each other. As a result, the surface became rough and coarse. Fig. 3c shows the SEM image of ZMCN after dye degradation. It could be seen from the image that the physical nature of the catalyst has changed. The distribution of heavy metals in the composite was confirmed by energy-dispersive X-ray spectroscopy (EDX) analysis, as shown in Fig. 3d. The percentage of carbon, oxygen, Cu, and Ni was 20%, 50%, 2%, and 3%, respectively (Table 1).

3.3. High-resolution transmission electron microscopy analysis

The size and physical characteristics of ZMCN nanoparticles were revealed by high-resolution transmission electron microscopy (HR-TEM), as shown in Fig. 4. The activated carbon matrix appeared brighter in transmission electron microscopy (TEM) images owing to the contrast.

HR-TEM demonstrated that the metal in ZMCN was in a highly diffused state. It might be owing to the carbon matrix's high particle density. The nanoparticle in ZMCN was visible in HR-TEM techniques, and the material had a

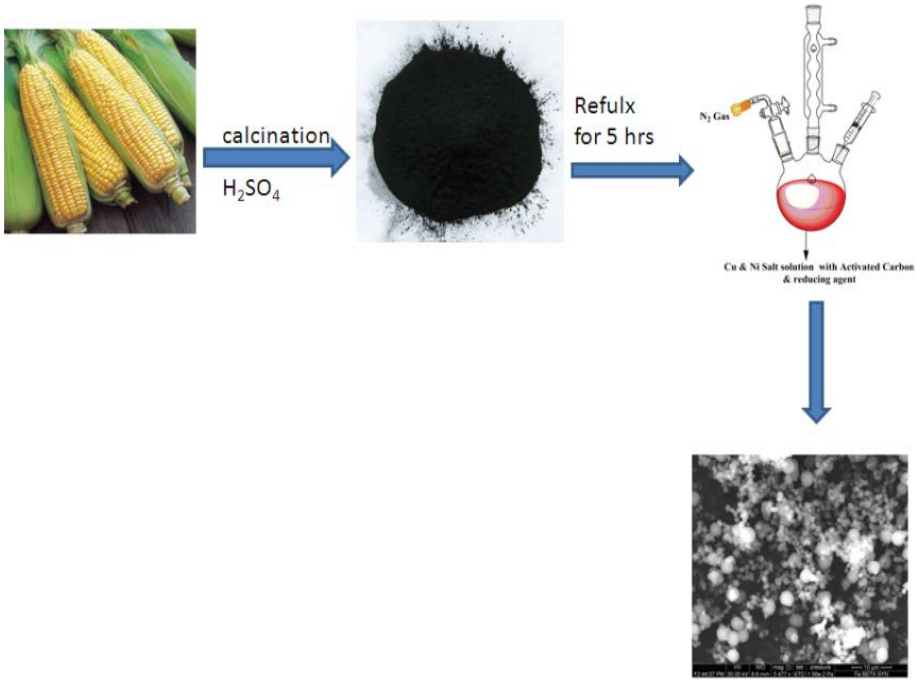

Fig. 1. Flowchart for preparation of activated carbon.

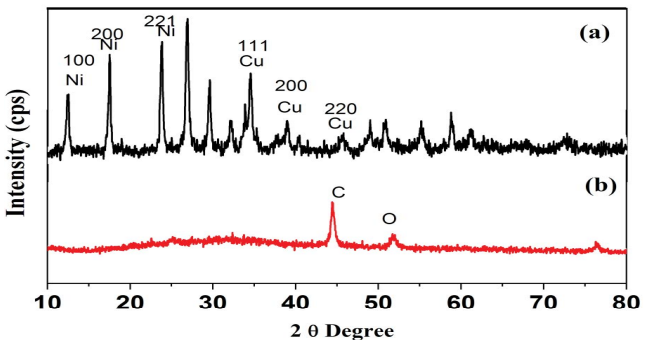

Fig. 2. XRD studies of (a) ZMCN composite and (b) activated carbon.

characteristic form. The ZMCN nanoparticles were between 30 and 50 nm in size.

3.4. FT-IR studies

The FT-IR technique is a helpful tool for identifying key functional groups on the surfaces of materials that can absorb organic contaminants. Fig. 5 shows the FT-IR spectra of the activated carbon and ZMCN. FT-IR spectra of activated carbon (Fig. 5b) show strong bands at around 3,500 cm^{-1} which can be attributed to O–H groups. Stretching vibrations of aliphatic groups $–CH_2–$ caused the band to appear at around 2,920 cm^{-1}. Conjugated C=O stretching or C–O stretching in carboxyl groups can be assigned to the bands at roughly 1,500 and 1,750 cm^{-1}, respectively. C–O stretching of carboxylate and ether compounds was responsible for FT-IR peaks at 1,200 cm^{-1}. Thus, it could be concluded that activated carbon has a lot of functional groups for adsorbing harmful ions. These functional groups play an essential role in contaminant ion adsorption [21]. The FT-IR spectrum of the synthesized ZMCN is given in Fig. 5a, and there is a drastic shift in the absorption peak, which might be due to the metal oxide ion impregnation in the activated carbon. The presence of six prominent peaks at 3,337.25; 1,656.45; 1,452.55; 1,398.69; 1,163.39 and 1,097.44 cm^{-1}, which represent O–H stretching vibrations (alcoholic or phenolic), C–H asymmetric stretching, C=C stretching, C=C aromatic ring stretching, C–OH stretching vibrations and C–OH bending, respectively, as revealed in Fig. 5a.

3.5. BET analysis

Fig. 6a shows nitrogen adsorption–desorption isotherms on the ZMCN, revealing a type IV isotherm for activated carbon, which is classified as mesoporous support by the IUPAC. Fig. 6b shows the surface area and total pore volume of the catalysts acquired by BET. The surface area of the BET dropped as the metal concentration increased, as the pores of the activated carbon were plugged by the precipitating copper and nickel ions, lowering the surface area available for nitrogen adsorption over the support. ZMCN had a surface area of 1,256 m^2/g and a total pore volume of 0.245 mL/g.

3.6. TGA/DTA studies

Fig. 7 shows the thermogravimetric analysis findings for the ZMCN nanocomposite. In ZMCN, there were two distinct weight loss regions. The water in the catalyst was initially lost, which corresponded to a weight loss between 30°C and 120°C. Since then, weight loss does not commence until the temperature reaches 350°C. At this temperature,

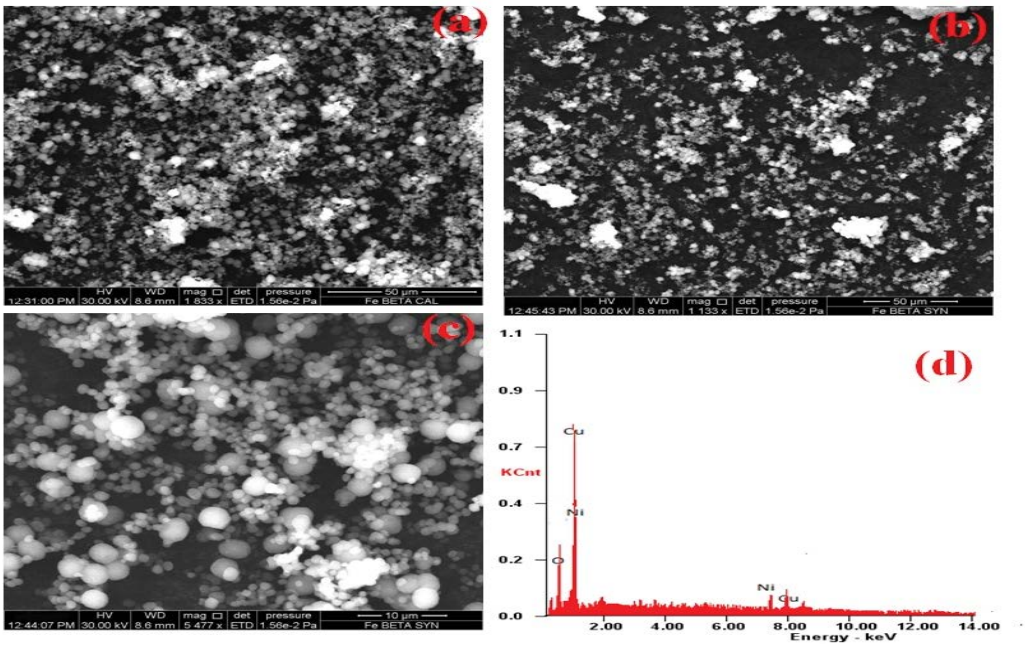

Fig. 3. SEM image of (a) activated carbon, (b) ZMCN nanocomposite, (c) ZMCN catalyst after dye degradation d. EDX image.

Table 1
EDX datas for composition metal with activated carbon

Element	wt.%	at.%
OK	10.15	50.16
CK	3.40	20.28
CuK	1.20	1.72
NiK	1.82	2.42
Matrix	Correction	ZAF

the catalyst does not degrade. After 350°C, the activated carbon began to break down, and the volatiles were released. Decomposition-induced weight loss continued upto 480°C. All the volatiles decomposed between 350°C and 480°C. As observed, the activated carbon decomposed at this temperature, whereas the metal oxide remained stable and did not decompose. After 500°C, there was no apparent change in weight, indicating the stability of the Cu/NiO nanoparticle.

3.7. Photodegradation studies

3.7.1. Dye concentration studies

Fig. 8 depicts the absorption spectrum of Rhodamine B (RhB) at various time intervals and concentrations with ZMCN catalyst. The solution was agitated with a magnetic stirrer under UV light; after 10mg of ZMCN was added to 10 mL of 25, 50, and 75 ppm RhB solution. Fig. 9 depicts the removal rate of RhB at various concentrations. The dye degradation rate was accelerated using UV light. The dye solution's percent removal was measured regularly. The 25 ppm solution degraded 98.1% in 110 min, while the 75 ppm solution took 110 min to degrade to 70.5%. After 110 min, the degradation remained constant, indicating that equilibrium had been reached. With increased concentration, the degradation decreased because the UV light was blocked by the higher concentration of the RhB dye, and the active site for the degradation on ZMCN decreased due to overcrowding on the surface, hence the degradation decreases. Thus, with an increase in concentration, the degradation time increases, and the percent degradation also decreases.

A kinetic study was carried out to determine the order of the degradation reaction of ZMCN on RhB. It was found that the degradation of RhB by ZMCN followed pseudo-first-order kinetics. Pseudo-first-order rate constant k was calculated using Eq. (1):

$$\ln\frac{C_o}{C_t} = kt \tag{1}$$

where C_o is the initial concentration of the solution and C_t is the concentration of RhB after t min, k is the pseudo-first-order rate constant. The slope of the graph gives the value of k in min^{-1}. The R^2 value for the plot (Fig. 10) was found to be 0.97, which indicates the degradation follows pseudo-first-order kinetics. Therefore, the value k for degradation was found to be 0.03187 min^{-1} for the degradation of RhB.

3.7.2. Effect of UV light irradiation time

The dye degradation by ZMCN increased when the solution was irradiated with UV light. Without the UV light, the degradation was found to happen very slowly. For example, 25 ppm solution was found to degrade up to only 34% (time 70 min) without UV light, but in the presence of the UV light, the dye degraded 98.1%. Furthermore,

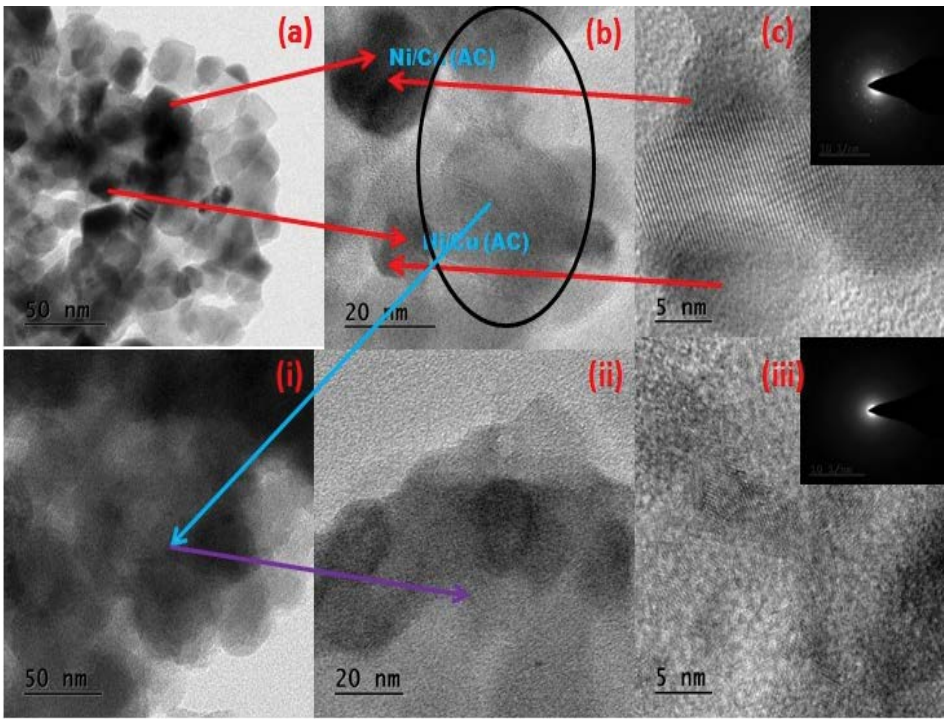

Fig. 4. HR-TEM image for ZMCN nanocomposite.

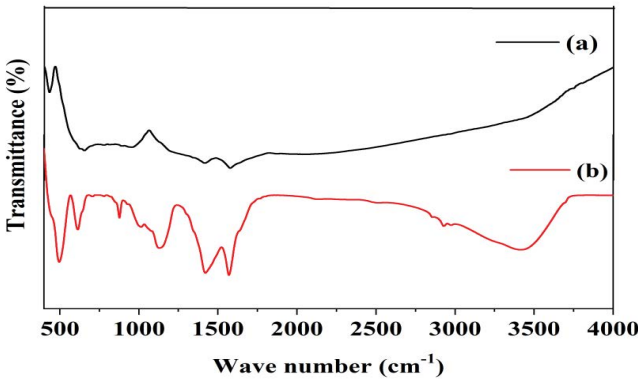

Fig. 5. FT-IR graph of a. ZMCN nanocomposite b. activated carbon.

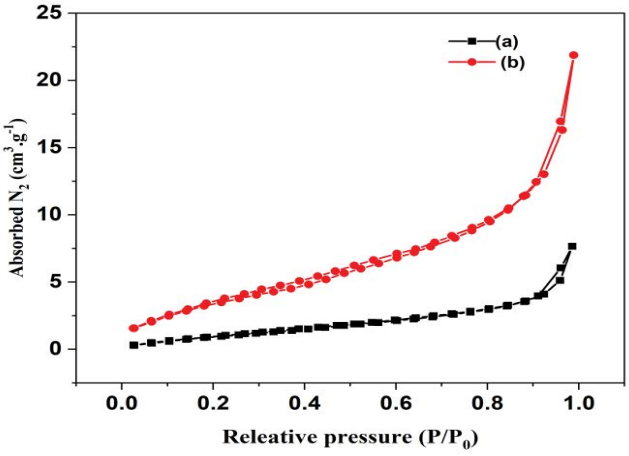

Fig. 6. BET analysis of (a) activated carbon and (b) ZMCN nanocomposite.

irradiation time increased with an increase in the concentration, as shown in Fig. 9. For example, the time taken for 50 ppm solution to attain maximum degradation was 90 min, whereas, for 75 ppm, the time was 110 min to attain the maximum degradation. With an increase in the dye concentration, the removal percent was found to be very low (around 40%) after irradiating with UV light for up to nearly 2 h.

3.7.3. Effect of pH on degradation

pH plays a vital role in dye degradation and adsorption [27]. RhB gets protonated at lower pH and dimerized at higher pH; hence the activity of the composite depends on the medium pH. This study shows an interesting trend, as the removal of RhB was found to be low at acidic pH. The effect of the removal of RhB on the pH of the solution is depicted in Fig. 11. With an increase in pH, the removal also increased and reached a maximum value at pH 9, and with a further increase in pH, there was a slight decrease in the removal percent. High pH values result in a higher concentration of hydroxyl ions, and the hydroxyl ion was found to activate ZMCN, resulting in a faster photocatalytic decolorization rate of dyes [28]. However, if the pH increases beyond 10, the dimerization of RhB occurred and hence the dye degradation decreases slightly.

3.7.4. Effect of adsorbent dosage

The number of active sites for dye degradation increased with an increase in the adsorbent mass [29]. A total of

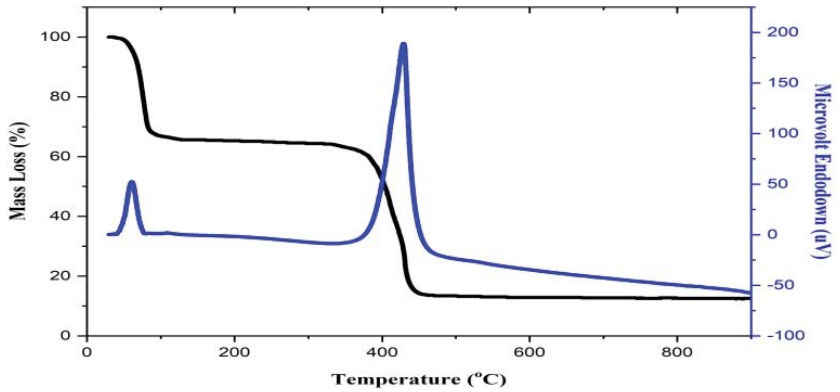

Fig. 7. TGA/DTA spectrum of ZMCN nanocomposite.

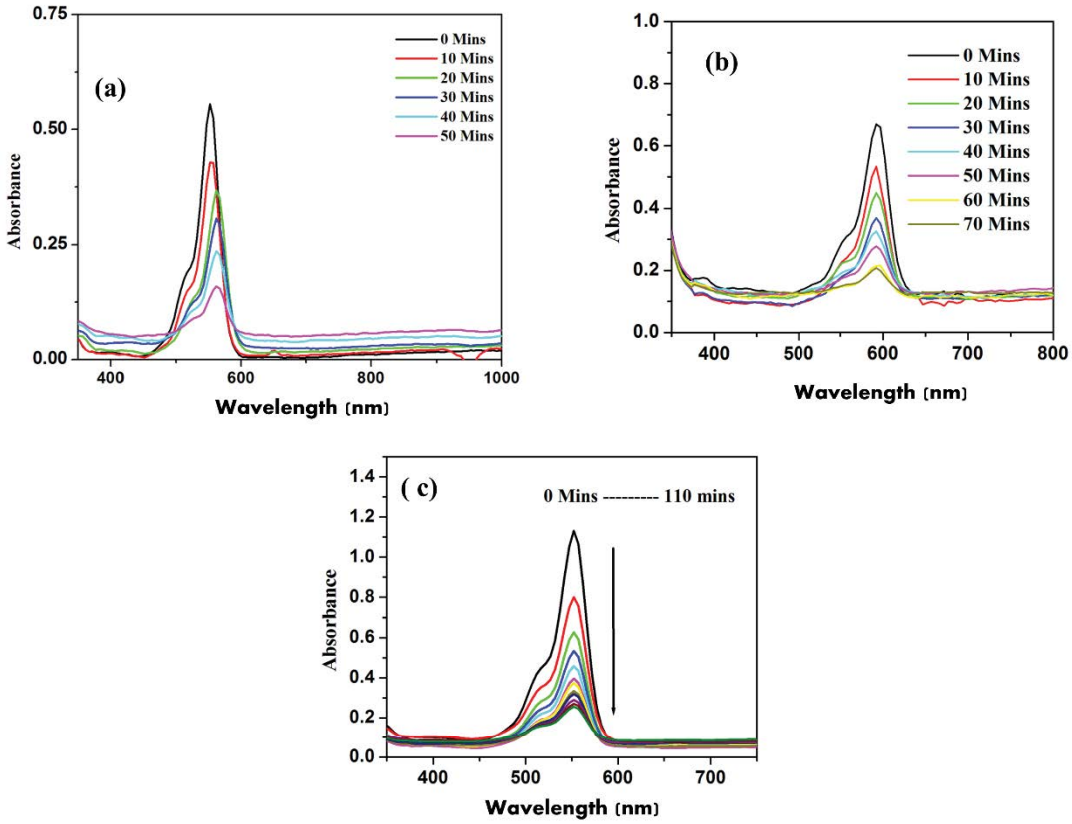

Fig. 8. UV-Visible spectrum of dye removal by ZMCN nanocomposite at (a) 25 ppm, (b) 50 ppm and (c) 75 ppm.

10 mL of a 100 ppm solution was utilized with various amounts of adsorbent ranging from 10 to 100 mg. The irradiation duration was 75 min. Fig. 12 demonstrates how removal percent changed as the adsorbent mass increases. For 10 and 100 mg of adsorbent, the removal rate increased from 20% to roughly 90% as the mass of the adsorbent increased. It could be explained that an increase in the active site of the catalyst had led to a more efficient degradation.

3.7.5. Reactive species involved in degradation of RhB dye

The degradation of a dye by a metal catalyst typically follows the redox mechanism. Irradiation of the light on the metal catalyst would excite an electron from its lattice site, and there would be a formation of an excited electron which would be present in the conduction band (e^-). Holes would be produced at the valence band (h^+). The e^- in the conduction band and h^+ generated the active species that cause the degradation of RhB. The e^- and h^+ reacted with the oxygen, and the water adsorbed on the surface.

The e^- would reduce oxygen that was adsorbed on the ZMCN, leading to the formation of $^{\bullet}O_2^-$ superoxide anion radical. $^{\bullet}O_2^-$ may further react with water leading to the formation of many other reactive species like H_2O_2, $^{\bullet}OOH$, and $^{\bullet}OH$ (hydroxyl radical). The holes that were formed acted as an oxidizing site and oxidize the hydroxide ion

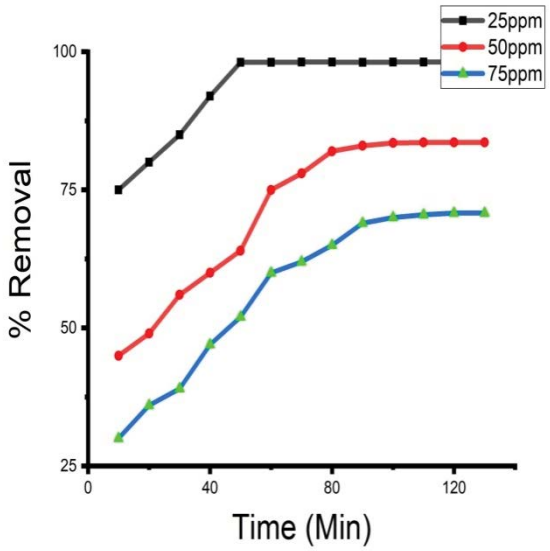

Fig. 9. Dye removal by ZMCN nanocomposite at various time intervals.

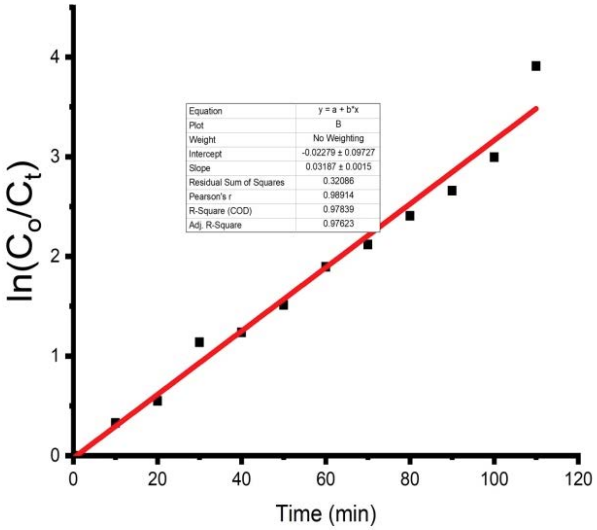

Fig. 10. Degradation study of RhB by ZMCN in a pseudo-first-order kinetics (concentration 25 ppm).

(OH^-) present in the solution to hydroxyl radical ($^•OH$). The intermediates produced from oxidation and reduction act as active species and can react with RhB. The RhB then would be reduced or oxidized, resulting in the degradation. The e-scavenger used in this work is 1 mL of 1 mM $AgNO_3$ in 10 mL dye solution, and sodium oxalate of the same strength and quantity was used for studying the scavenging activity of h^+. Fig. 13 shows the percent removal of RhB dye with various scavengers. It can be seen from Fig. 13 that the percent removal of RhB was considerably reduced by the addition of oxalate compared to scavenging activity of $AgNO_3$, indicating that holes, h^+ played a vital role in degradation reaction compared to

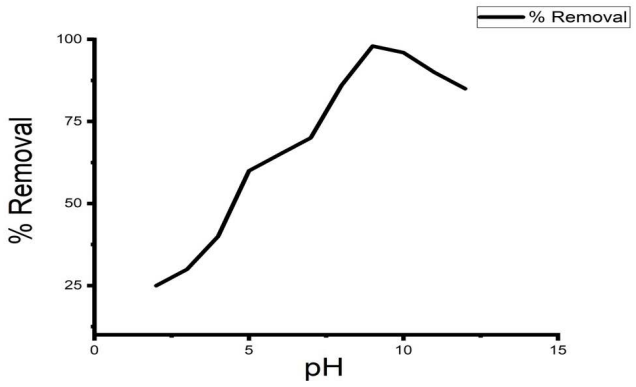

Fig. 11. Variation of removal of RhB with pH of the solution by ZMCN composite.

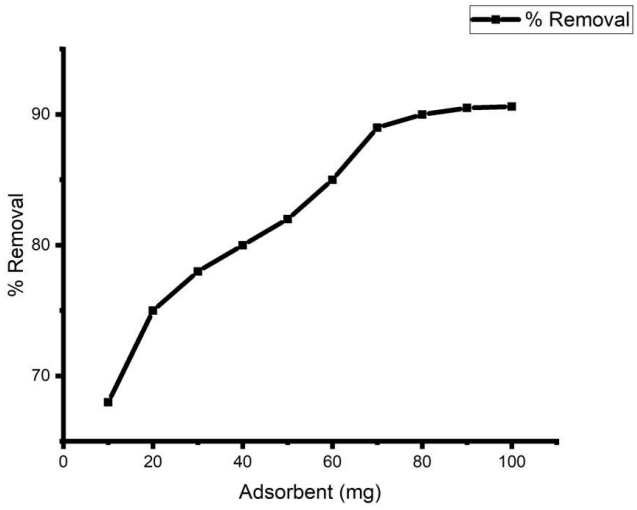

Fig. 12. Variation of removal percent with adsorbent mass.

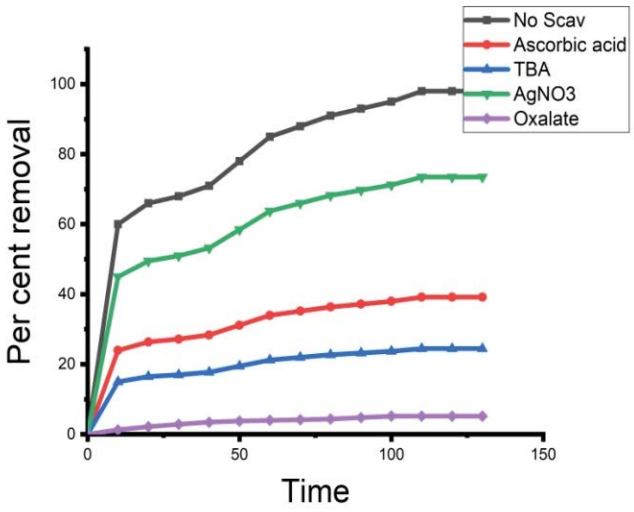

Fig. 13. Removal percent of RhB in presence of various scavengers.

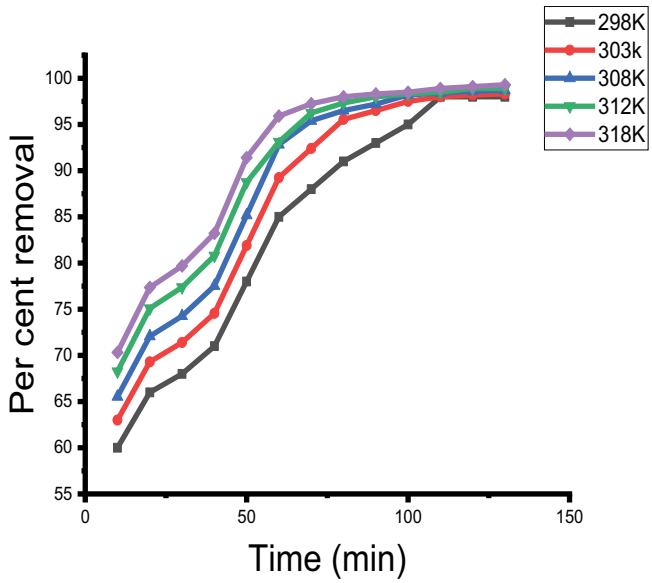

Fig. 14. Effect of temperature on the percent removal of RhB by ZMCN in 10 mL of 50 ppm solution.

e^-. Nonetheless, both the h^+ and e^- scavengers reduced the percent removal of RhB, showing that the RhB underwent both oxidation and reduction. However, the oxidation process was more prominent than the dye reduction reaction. The radical that influenced the degradation process was also checked with ascorbic acid, as an $^{\bullet}O_2^-$ scavenger and for $^{\bullet}OH$ tert-butanol (TBA) was used [30–33]. TBA inhibits the degradation more effectively than ascorbic acid. Hence the degradation of the RhB can be carried out by the holes and hydroxyl radicals. The following mechanism was proposed considering the above discussion.

Formation of active species:

$Cu/NiO + UV\ light \rightarrow e^- + h^+$ (formation of holes and electron)

$h^+ + H_2O \rightarrow {}^{\bullet}OH + H^+$(oxidation of water)

$O_2 + e^- \rightarrow {}^{\bullet}O_2^-$ (reduction of oxygen)

$H_2O + {}^{\bullet}O_2^- \rightarrow H_2O_2$(oxidation of water)

$e^- + H_2O_2 \rightarrow {}^{\bullet}OH$ (reduction of peroxide)

Degradation reaction of dye (main reaction)

$RhB + h^+ \rightarrow$ Oxidized product

$RhB + {}^{\bullet}OH \rightarrow$ Oxidized product + OH^-

3.7.6. Effect of temperature

With an increase in temperature, the rate of the chemical reaction increased (Fig. 14). The effect of temperature on the degradation of RhB was analyzed in 50 ppm of dye solution at various temperatures. With an increase in temperature, the degradation appeared to increase. At 45°C, the degradation reaction was completed in 80 min, whereas the same took 110 min at 25°C. With an increase in temperature, the rate of the reaction increased and catalytic activity for the degradation also increased.

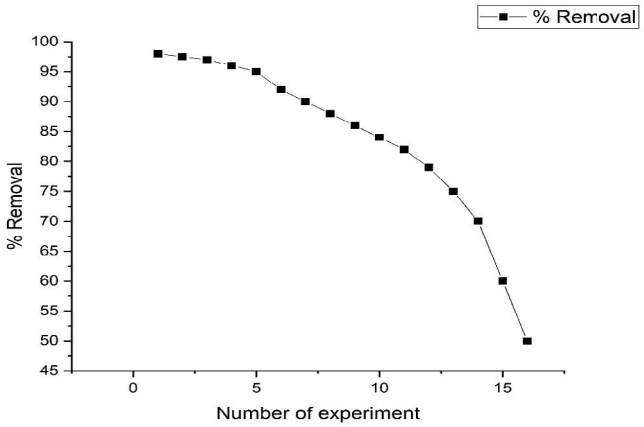

Fig. 15. Reusability of the catalyst (number of experiments in 100).

3.8. Catalyst's durability

The reusability of the catalyst was carried out by recovering the catalyst after the degradation reaction using the centrifugation technique. The solution, after degradation, was centrifuged at 500 rpm in a test tube. The supernatant solution was discarded, the catalyst was washed with 5 mL of double-distilled water several times, and then the catalyst was dried at room temperature for an hour. It was found that the efficiency of the catalyst decreased after 500 experiments, as shown in Fig. 15. The recovery percentage after each experiment was found to be 99.5%.

4. Conclusion

Novel nanocomposite materials combining an activated carbon using *Zea mays* L. waste and a transition metal (NiO, Cu) using a very simple impregnation process are synthesized in this work. The synthesized nanocomposites show high porosity. XRD and TEM images show high crystallization of the metal in the composite. The ZMCN composite is tested for the degradation of the Rhodamine B and found to be effective in degrading the dye. pH for the dye degradation is found to be 9, and is observed that with an increase in the adsorbent mass, the degradation also increases.

References

[1] Y.Y. Si, J.N. Li, B. Cui, D.J. Tang, L. Yang, V. Murugadoss, S. Maganti, M. Huang, Z.H. Guo, Janus phenol–formaldehyde resin and periodic mesoporous organic silica nanoadsorbent for the removal of heavy metal ions and organic dyes from polluted water, Adv. Compos. Hybrid Mater., 5 (2022) 1180–1195.
[2] A. Umar, M.M. Rahman, A. Al-Hajry, Y.-B. Hahn, Enzymatic glucose biosensor based on flower-shaped copper oxide

nanostructures composed of thin nanosheets, Electrochem. Commun., 11 (2009) 278–281.
[3] W.S. Choi, H.-J. Lee, Nanostructured materials for water purification: adsorption of heavy metal ions and organic dyes, Polymers (Basel), 14 (2022) 2183, doi: 10.3390/polym14112183.
[4] A. Hadi Abdullah, R. Mat, S. Somderam, A. Shah Abd Aziz, M. Abu Asshaary Daud, H_2S adsorption using ZnO modified Na-A zeolite and conditions optimization by response surface methodology, J. Phys. Conf. Ser., 2266 (2022) 012006, doi: 10.1088/1742-6596/2266/1/012006.
[5] S.-J. Hong, H.-J. Mun, B.-J. Kim, Y.-S. Kim, Characterization of nickel oxide nanoparticles synthesized under low temperature, Micromachines, 12 (2021) 1168, doi: 10.3390/mi12101168.
[6] H. Li, Y. Li, R. Wang, R. Cao, Synthesis and electrochemical capacitor performance of mesostructured nickel oxide/carbon composites by a co-casting method, J. Alloys Compd., 481 (2009) 100–105.
[7] A. Asfaram, M. Ghaedi, S. Hajati, A. Goudarzi, A.A. Bazrafshan, Simultaneous ultrasound-assisted ternary adsorption of dyes onto copper-doped zinc sulfide nanoparticles loaded on activated carbon: optimization by response surface methodology, Spectrochim. Acta, Part A, 145 (2015) 203–212.
[8] M. Iwanow, T. Gärtner, V. Sieber, B. König, Activated carbon as catalyst support: precursors, preparation, modification and characterization, Beilstein J. Org. Chem., 16 (2020) 1188–1202.
[9] R. Kupila, K. Lappalainen, T. Hu, H. Romar, U. Lassi, Lignin-based activated carbon-supported metal oxide catalysts in lactic acid production from glucose, Appl. Catal., A, 612 (2021) 118011, doi: 10.1016/j.apcata.2021.118011.
[10] S. Anbazhagan, V. Thiruvengatam, K. Kulanthai, Adaptive neuro-fuzzy inference system and artificial neural network modeling for the adsorption of methylene blue by novel adsorbent in a fixed-bed column method, Iran. J. Chem. Chem. Eng., 39 (2020) 75–93.
[11] S. Anbazhagan, V. Thiruvengadam, A. Sukeri, An Amberlite IRA-400 Cl^- ion-exchange resin modified with *Prosopis juliflora* seeds as an efficient Pb^{2+} adsorbent: adsorption, kinetics, thermodynamics, and computational modeling studies by density functional theory, RSC Adv., 11 (2021) 4478–4488.
[12] M. Auta, B.H. Hameed, Acid modified local clay beads as effective low-cost adsorbent for dynamic adsorption of methylene blue, J. Ind. Eng. Chem., 19 (2013) 1153–1161.
[13] S.-L. Liu, Y.-N. Wang, K.-T. Lu, Preparation and pore characterization of activated carbon from Ma bamboo (*Dendrocalamus latiflorus*) by H_3PO_4 chemical activation, J. Porous Mater., 21 (2014) 459–466.
[14] J.M.V. Nabais, C. Laginhas, M.M.L.R. Carrott, P.J.M. Carrott, J.E.C. Amorós, A.V.N. Gisbert, Surface and porous characterisation of activated carbons made from a novel biomass precursor, the esparto grass, Appl. Surf. Sci., 265 (2013) 919–924.
[15] A. Policicchio, E. Maccallini, R.G. Agostino, F. Ciuchi, A. Aloise, G. Giordano, Higher methane storage at low pressure and room temperature in new easily scalable large-scale production activated carbon for static and vehicular applications, Fuel, 104 (2013) 813–821.
[16] B. Meryemoglu, S. Irmak, A. Hesenov, O. Erbatur, Preparation of activated carbon supported Pt catalysts and optimization of their catalytic activities for hydrogen gas production from the hydrothermal treatment of biomass-derived compounds, Int. J. Hydrogen Energy, 37 (2012) 17844–17852.
[17] P. Samiyammal, A. Kokila, L.A. Pragasan, R. Rajagopal, R. Sathya, S. Ragupathy, M. Krishnakumar, V.R. Minnam Reddy, Adsorption of brilliant green dye onto activated carbon prepared from cashew nut shell by KOH activation: studies on equilibrium isotherm, Environ. Res., 212 (2022) 113497, doi: 10.1016/j.envres.2022.113497.
[18] M. Sultana, M.H. Rownok, M. Sabrin, M.H. Rahaman, S.M.N. Alam, A review on experimental chemically modified activated carbon to enhance dye and heavy metals adsorption, Cleaner Eng. Technol., 6 (2022) 100382, doi: 10.1016/j.clet.2021.100382.
[19] J. Lin, S. Zhao, S. Cheng, Microwave-assisted preparation of cotton stem-derived activated carbon for dye removal from synthetic wastewater, Environ. Sci. Pollut. Res., 29 (2022) 48839–48850.
[20] S. Soroush, N.M. Mahmoodi, B. Mohammadnezhad, A. Karimi, Activated carbon (AC)-metal-organic framework (MOF) composite: synthesis, characterization and dye removal, Korean J. Chem. Eng., 39 (2022) 2394–2404.
[21] E. Kaçan, C. Kütahyalı, Adsorption of strontium from aqueous solution using activated carbon produced from textile sewage sludges, J. Anal. Appl. Pyrolysis, 97 (2012) 149–157.
[22] A.M. Mansour, E.M. El Bakry, N.T. Abdel-Ghani, Photocatalytic degradation of methylene blue with copper(II) oxide synthesized by thermal decomposition of flubendazole complexes, J. Photochem. Photobiol., A, 327 (2016) 21–24.
[23] A. Sivaprakasam, T. Venugopal, Modelling the removal of Lead from synthetic contaminated water by activated carbon from biomass of *Diplocyclos palmatus* by RSM, Global Nest J., 21 (2019) 319–327.
[24] J. Shu, S. Cheng, H. Xia, L. Zhang, J. Peng, C. Li, S. Zhang, Copper loaded on activated carbon as an efficient adsorbent for removal of methylene blue, RSC Adv., 7 (2017) 14395–14405.
[25] S.D. Khairnar, V.S. Shrivastava, Facile synthesis of nickel oxide nanoparticles for the degradation of Methylene blue and Rhodamine B dye: a comparative study, J. Taibah Univ. Sci., 13 (2019) 1108–1118.
[26] A. Omidvar, B. Jaleh, M. Nasrollahzadeh, Preparation of the GO/Pd nanocomposite and its application for the degradation of organic dyes in water, J. Colloid Interface Sci., 496 (2017) 44–50.
[27] M.H. Chou, S.B. Liu, C.Y. Huang, S.Y. Wu, C.L. Cheng, Confocal Raman spectroscopic mapping studies on a single CuO nanowire, Appl. Surf. Sci., 254 (2008) 7539–7543.
[28] G.F. Cai, J.P. Tu, J. Zhang, Y.J. Mai, Y. Lu, C.D. Gu, X.L. Wang, An efficient route to a porous NiO/reduced graphene oxide hybrid film with highly improved electrochromic properties, Nanoscale, 4 (2012) 5724–5730.
[29] R. Sangeetha Piriya, R.M. Jayabalakrishnan, M. Maheswari, K. Boomiraj, S. Oumabady, Coconut shell derived $ZnCl_2$ activated carbon for malachite green dye removal, Water Sci. Technol., 83 (2021) 1167–1182.
[30] K. Kabra, R. Chaudhary, R.L. Sawhney, Treatment of hazardous organic and inorganic compounds through aqueous-phase photocatalysis: a review, Ind. Eng. Chem. Res., 43 (2004) 7683–7696.
[31] C.-Y. Chu, M.H. Huang, Facet-dependent photocatalytic properties of Cu_2O crystals probed by using electron, hole and radical scavengers, J. Mater. Chem. A, 5 (2017) 15116–15123.
[32] M.A. Islam Molla, I. Tateishi, M. Furukawa, H. Katsumata, T. Suzuki, S. Kaneco, Evaluation of reaction mechanism for photocatalytic degradation of dye with self-sensitized TiO_2 under visible light irradiation, Open J. Inorg. Non-met. Mater., 7 (2017) 1–7.
[33] T. An, J. An, H. Yang, G. Li, H. Feng, X. Nie, Photocatalytic degradation kinetics and mechanism of antivirus drug-lamivudine in TiO_2 dispersion, J. Hazard. Mater., 197 (2011) 229–236.